



**HAL**  
open science

# Numerical simulations of multi-phase electro-hydrodynamics flows using a simple incompressible smoothed particle hydrodynamics method

F. Almasi, M.S. Shadloo, A. Hadjadj, M. Ozbulut, N. Tofighi, M. Yildiz

► **To cite this version:**

F. Almasi, M.S. Shadloo, A. Hadjadj, M. Ozbulut, N. Tofighi, et al.. Numerical simulations of multi-phase electro-hydrodynamics flows using a simple incompressible smoothed particle hydrodynamics method. *Computers & Mathematics with Applications*, 2019, 10.1016/j.camwa.2019.10.029. hal-02383860

**HAL Id: hal-02383860**

**<https://hal.science/hal-02383860>**

Submitted on 2 Jan 2023

**HAL** is a multi-disciplinary open access archive for the deposit and dissemination of scientific research documents, whether they are published or not. The documents may come from teaching and research institutions in France or abroad, or from public or private research centers.

L'archive ouverte pluridisciplinaire **HAL**, est destinée au dépôt et à la diffusion de documents scientifiques de niveau recherche, publiés ou non, émanant des établissements d'enseignement et de recherche français ou étrangers, des laboratoires publics ou privés.



Distributed under a Creative Commons Attribution - NonCommercial 4.0 International License

# Numerical simulations of multi-phase electro-hydrodynamics flows using a simple incompressible smoothed particle hydrodynamics method

F. Almasi<sup>1</sup>, M. S. Shadloo<sup>1,2,\*</sup>, A. Hadjadj<sup>1</sup>, M. Ozbulut<sup>3</sup>, N. Tofighi<sup>4</sup>, M. Yildiz<sup>4,5,6</sup>

<sup>1</sup> *CORLA - UMR 6614, Normandie University, CNRS - INSA of Rouen, 76000 Rouen, France*

<sup>2</sup> *Institute of Chemical Process Engineering, University of Stuttgart, Stuttgart, 70199, Germany*

<sup>3</sup> *Engineering Faculty, Piri Reis University, 34940 Istanbul, Turkey*

<sup>4</sup> *Sabancı University, Faculty of Engineering and Natural Sciences, Tuzla, 34956, Istanbul, Turkey*

<sup>5</sup> *Integrated Manufacturing Technologies Research and Application Center, Sabancı University, Tuzla, 34956, Istanbul, Turkey*

<sup>6</sup> *Composite Technologies Center of Excellence, Sabancı University-Kordsa, Istanbul Technology Development Zone, Sanayi Mah. Teknopark Blvd. No: 1/1B, Pendik, 34906, Istanbul, Turkey*

---

## Abstract

Practically, every processing technology deals with complex multi-phase flows and predicting the fluid flow behaviour is crucial for these processes. Current study discusses the application of a mesh-less numerical methodology, i.e. Incompressible Smoothed Particle Hydrodynamics (ISPH) to investigate the behaviour of different multi-phase flow systems. This work is presented in a coherent way with increasing test problem difficulties and their concerned physical complexities. A wide range of problems including Laplace's law, bubble rising, bubble suspension under an external electric field are considered for a code validation purpose, while the numerical results manifest very good accordance with the experimental and theoretical data. Finally, we show the effectiveness of using an external electric field for controlling a complex problem such as Couette flow for a range of electrical permittivity and electrical conductivity ratios. It is noted that the Electrohydrodynamics (EHD) effect on a suspended droplet in Couette flow case is simulated for the first time using the SPH method.

*Keywords:* Smoothed Particle Hydrodynamics (SPH), Meshless methods, ElectroHydrodynamics (EHD), Multi-phase flow, Couette flow

---

## 1 1. Introduction

2 Predicting the behaviour of multi-phase flow systems has attracted for decades the atten-  
3 tion of many industries due to their wide ranges of applications in the chemical engineering,  
4 aerospace engineering and renewable energy sectors, among others [1, 2, 3]. In multi-phase sys-  
5 tems two or more fluids share interfaces which can deform/ migrate as outcome of exerted forces  
6 and constitutional laws. Some applications of multi-phase systems include boiling, condensa-  
7 tion, water purification and petroleum refinement processes where these phenomena have been  
8 investigated mostly experimentally and theoretically. However, with the ever-increasing power  
9 of Computational Fluid Dynamics (CFD) methods, numerical simulations of these systems be-  
10 came of great interest among researchers [4, 5, 6].

11 Smoothed Particle Hydrodynamics (SPH) is a relatively recent and promising mesh-less La-  
12 grangian method which discretizes the domain into a set of nodes, known as material particles.  
13 These particles can freely move inside the computational domain subject to an external force or  
14 particle-particle interactions. Initially introduced by Gingold and Monaghan [7], and Lucy [8]  
15 for astrophysics applications, SPH was soon found to be suitable for fluid dynamics problems,  
16 where complex geometries [9, 10, 11], large deformations [12, 13, 14], multi-phase [15, 16, 17] and  
17 multi-physics problems [18, 19, 20] are involved. A recent overview for the application of SPH  
18 can be found in [21].

19 One of the most important engineering problems which involves many of above cases is the  
20 Electrohydrodynamics (EHD) one, where hydrodynamics of a fluid system is coupled with its  
21 response to an external electric field. In EHD problems, one may control the interface between  
22 the two fluids (here, the droplet and the bulk fluid) by controlling the flow conditions and fluid  
23 properties [22, 23]. In such problems, the coupling may lead to a large interfacial deformation  
24 (i.e. merge/breakup) or migration. Indeed, EHD is a very complex problem including multi-  
25 phase, multi-physics and multi-scale phenomena with strong topological changes of the interface  
26 shape [24, 25]. Although, there are many experimental and theoretical studies available in the  
27 literature on the coupled modeling of EHD problems [26, 27, 28]. Nevertheless, some discrep-  
28 ancies between experiments and analytical data still exist [28]. As such, numerical simulations  
29 have been developed to tackle these difficulties and provide insight into EHD problems.

30 Considering the numerical simulations of EHD using SPH method, Shadloo et al. [29] were  
31 the first group to provide a model for such problems. They validated their code with the simple  
32 EHD deformation of droplets suspended in a neutrally buoyant Newtonian fluid. Rahmat et  
33 al. have proposed a multi phase ISPH method based on the lubrication theory and the drainage  
34 model to simulate droplet electro-coalescence for wide ranges of simulation conditions. [30, 31].  
35 Rahmat et al. [32] also provided the first simulation results for the Rayleigh-Taylor instability  
36 under the combined effect of electric field and gravitational forces. Yet, step-by-step validation of  
37 the SPH method for each individual force using the same methodology is not well-documented.  
38 Additionally, numerical simulation of a multi-phase flow under the effects of an electric field

39 using various scenarios ranging from low to high deformations, droplet migration, and effect of  
 40 shear flow on the droplet's deformation would provide a broader perspective into the capabilities  
 41 of the SPH method for such applications. To this end, this article aims at introducing a **mesh-less**  
 42 **numerical methodology, i.e.** Incompressible SPH (ISPH) approach, to deal with such complex  
 43 problems. Additionally, we verify the applicability of some of the used algorithms for a range of  
 44 problems including hydrodynamic, capillary, gravity, shear and EHD forces.

45 This article is organized as follows: First, we introduce the mathematical formulation of the  
 46 SPH method as well as the numerical discretization scheme. Then, we incorporate the governing  
 47 equations of the multi-phase system including the conservation equations for mass, momentum  
 48 and electrical charges in a Lagrangian form. Thereafter, a code validation and numerical conver-  
 49 gence study is asserted in the absence of electric field. Numerical results cover solutions with  
 50 and without electric field sections. Additionally, the effect of surface tension through Laplace  
 51 law, the effect of gravitational force, and the Couette flow for a multi-phase system are examined  
 52 and validated against analytical solution and available numerical data in the literature. Finally,  
 53 conclusions are provided in the last section.

## 54 2. Mathematical Formulation of SPH

55 The idea of SPH comes from the fact that any field variable  $f(x)$  can be calculated by an  
 56 exact mathematical relation as

$$f(x) = \int_{\Omega} f(x')\delta(x')dx'. \quad (1)$$

57 Upon approximating  $\delta(x')$  by an interpolation function  $W(x - x', h)$ , this equation can be for-  
 58 mulated as

$$f(x) = \int_{\Omega} f(x')W(x - x', h)dx', \quad (2)$$

59 where  $x$  and  $x'$  are the position vectors and  $h$  is the smoothing length. **In our case,  $h = \zeta dx$**   
 60 **where  $\zeta=1.6$  is a constant value, and  $dx$  is the initial particle spacing.** The interpolation func-  
 61 tion, also known as smoothing function or kernel function, should have, among others, the  
 62 following properties [33]

63 – Normalized over the domain

$$\int_{\Omega} W(x - x', h)dx = 1. \quad (3)$$

64 – Produces  $\delta$  function for a small enough smoothing length

$$\lim_{h \rightarrow 0} W(x - x', h) = \delta(x'). \quad (4)$$

- 65 – Remains monotonically decreasing throughout the entire domain.  
 66 – Has a compact support, meaning that for  $|x - x'| > kh$

$$W(x - x', h) = 0. \quad (5)$$

- 67 – Is a symmetric function.

68 Initially, the kernel functions were defined such that each particle should have interactions  
 69 with all others [7]. By introducing the concept of Neighboring particles<sup>1</sup>, kernel function affect  
 70 only a compact support around it were substituted (see Eq. (5)). **Depending on the smoothing**  
 71 **length parameter  $h$** , only a few number of particles in the entire space affect the approximated  
 72 value of the kernel function (around 25 to 35 in 2D). **In the current work, a cubic spline ker-**  
 73 **nel function is used both for the balk fluid and the interface modeling while taking harmonic**  
 74 **average.**

$$W_{ij} = A \begin{cases} 2/3 - (r/h)^2 + 1/2(r/h)^3 & r/h \in [0, 1) \\ 1/6(2 - r/h)^3 & r/h \in [1, 2). \\ 0 & r/h \geq 2 \end{cases} \quad (6)$$

75 Hereafter,  $W(x - x', h)$ , will be shown by  $W_{ij}$  and  $A = \frac{15}{7\pi h^2}$ . Also,  $i, j$ , and  $r$  represent the  
 76 index of the particle of interest, the index of its neighbors, and the smoothing radius.

77 To calculate the SPH gradients, one can show that it is sufficient to differentiate the kernel  
 78 function  $W(x - x', h)$ . In other words, in SPH there is no need to differentiate the field function  
 79  $f(x)$ ; instead one can differentiate the kernel function. The latter is one of the fascinating fea-  
 80 tures of the SPH method which distinguishes this method from other mesh-based techniques.  
 81 In this work, we use an improved version of the first derivative, presented in [34] as  
 82

$$\frac{\partial f_i^m}{\partial x_i^k} a_i^{kl} = \sum_j \frac{1}{\psi_j} (f_j^m - f_i^m) \frac{\partial W_{ij}}{\partial x_i^l}. \quad (7)$$

83 **Also, the derivatives for vectorial and scalar quantities are calculated, respectively, as follows:**  
 84

$$\frac{\partial^2 f_i^m}{\partial x_i^k \partial x_i^k} a_i^{ml} = 8 \sum_j \frac{1}{\psi_j} (f_i^m - f_j^m) \frac{\partial W_{ij}}{\partial x_i^l} \frac{r_{ij}^m}{r_{ij}^2}, \quad (8)$$

---

<sup>1</sup>particles that are located within the range of the kernel function with respect to the particle of interest. Outside of this range, the kernel function has already dropped to zero.

86 and

$$\frac{\partial^2 f_i}{\partial x_i^k \partial x_i^k} (2 + a_i^{kk}) = 8 \sum_j \frac{1}{\psi_j} (f_i - f_j) \frac{\partial W_{ij}}{\partial x_i^k} \frac{r_{ij}^k}{r_{ij}^2}, \quad (9)$$

87

88 where  $\psi$  is the particle number density and  $a_i^{kl}$  represents a corrective second rank tensor to  
89 avoid particle inconsistencies[9].

### 90 3. Governing Equations

91 Assuming an immiscible two-phase Newtonian, viscous, incompressible, isothermal fluid  
92 system, the corresponding mass and momentum conservations in a Lagrangian formulation are  
93 given as follows

$$\frac{D\rho}{Dt} = -\rho \nabla \cdot \vec{V}, \quad (10)$$

94 and

$$\rho \frac{D\vec{V}}{Dt} = \nabla \cdot \mathcal{T} + \vec{f}^b + \vec{f}^s + \vec{f}^e, \quad (11)$$

95 where,  $\rho$  is the fluid density,  $\frac{D}{Dt}$  is the material time derivative operator<sup>2</sup>,  $\nabla \cdot \vec{V}$  is the divergence  
96 of the velocity vector,  $\mathcal{T}$  is the total stress tensor which is defined as  $\mathcal{T} = -p\mathbf{I} + \tau$  where  $p$  is the  
97 static pressure,  $\mathbf{I}$  is the identity matrix and  $\tau = \mu(\nabla \vec{V} + (\nabla \vec{V})^T)$  is the viscous dissipation term  
98 for  $\mu$  being the dynamic viscosity.

99 Additionally,  $\vec{f}^b = \rho \vec{g}$  is the body force due to gravity and  $\vec{f}^s$  is the surface tension which can  
100 be calculated using the volumetric force proposed by Brackbill [35], so called the Continuum  
101 Surface Force (CSF) method, as

$$\vec{f}^s = \gamma \kappa \vec{n} \delta^s. \quad (12)$$

102 Here,  $\gamma$  is the surface tension coefficient,  $\kappa = -\nabla \cdot \vec{n}$  is the interface curvature,  $\vec{n} = \frac{\nabla C}{|\nabla C|}$  is the  
103 unit vector normal to the interface, and  $\delta^s = |\nabla C|$  is surface Dirac-delta function, and finally,  
104  $\vec{f}^e$  is the electric field force.

105 To avoid sharp discontinuities at the interface, the smoothed color function of the particle  $i$   
106 is defined as

$$C_i = \frac{\sum_j W_{ij} c_j}{\sum_j W_{ij}}, \quad (13)$$

107 where the color function  $c$  assigns a unit value to one phase and zero to the other phase in a  
108 two-phase system such that

---

<sup>2</sup>The material time derivative is a directional time derivative for a fixed point.

109

$$c_j = \begin{cases} 1, & \text{fluid A} \\ 0, & \text{fluid B} \end{cases}.$$

110 Furthermore, this approach provides a clear definition for the volume fraction of each fluid,  
 111 i.e.  $C_i^A = C_i$  and  $C_i^B = 1 - C_i$  define the volume fraction corresponding to the fluid A and  
 112 fluid B, respectively, such that  $\sum_n C_i^n = 1$  for all  $n$  phases, here  $n = 2$ .

113 As mentioned before, in this study the electrostatics and the hydrodynamics are coupled to-  
 114 gether. This coupling is achieved through the Maxwell stress tensor. Maxwell equations provide  
 115 a mathematical framework for the interaction and the connection between the electric and the  
 116 magnetic fields [36]. Here, the EHD part of the system can be regarded as quasi-static model,  
 117 and dynamic currents values are so low, hence the induced magnetic field effects are negligible.  
 118 Therefore, the contribution from the induced magnetic field is neglected. Consequently, the  
 119 volumetric electric force can be written as

$$\vec{f}^e = \nabla \cdot T^E. \quad (14)$$

120 In case of an application of the external electric field on a multi-phase fluid flow, this new  
 121 term for the electric force, will be added to the right hand side of the momentum equation (see  
 122 Eq. (11)), where the Maxwell's stress tensor defines as

$$T^E = \vec{D}\vec{E} - \frac{1}{2}(\vec{D} \cdot \vec{E})\mathbf{I}, \quad (15)$$

123 where  $\vec{E}$  is an external electric field,  $\vec{D} = \epsilon\vec{E}$  is the dielectric displacement vector, and  $\epsilon$  is  
 124 the electrical permittivity. Also, based on the Gauss's law [36]

$$\nabla \cdot \vec{D} = q^v, \quad (16)$$

125 where  $q^v$  is the free electric charge density.

126 Application of Eqs. (15) and (14) will result in

$$\vec{f}^e = q^v \vec{E} - \frac{1}{2} \vec{E} \cdot \vec{E} \nabla \epsilon. \quad (17)$$

127 In this work both fluids are considered to be leaky dielectric, (i.e. electric relaxation time is  
 128 much shorter compared to its viscous counterpart or  $t^e \ll t^v$ ).

#### 129 4. Time integration

130 We apply a predictor-corrector scheme to advance the governing flow equations in time con-  
 131 sidering a first-order Euler approach. The time-step is selected based on Courant-Friedrichs-  
 132 Lewy (CFL) condition in which  $\Delta t = C_{\text{CFL}} h / V_{\text{max}}$ , with  $V_{\text{max}}$  being the largest magnitude of

133 particle velocity and the  $C_{\text{CFL}}$  is the constant taken as 0.25. During the predictor step, we first  
 134 advance all the variables to an intermediate value denoted by (\*), from the variables' value at the  
 135  $n$ -th time-step denoted by superscript ( $n$ ), as

$$\vec{r}_i^* = \vec{r}_i^{(n)} + \vec{V}_i^{(n)} \Delta t + \delta \vec{r}_i^{(n)}, \quad (18)$$

$$\vec{V}_i^* = \vec{V}_i^{(n)} + \frac{\text{RHS}}{\rho_i^{(n)}} \Delta t, \quad (19)$$

$$\psi_i^{(*)} = \psi_i^{(n)} - \Delta t \psi_i^{(n)} (\nabla \cdot \vec{V}_i^*). \quad (20)$$

138 RHS denotes the right hand side of Eq. (11),  $\psi_i = \sum_j W_{ij}$ , is the number density asso-  
 139 ciated with the particle of interest  $i$ , which is calculated from the summation of kernel func-  
 140 tion at all neighboring particles  $j$ ,  $\delta r_i$  is the artificial particle displacement, defined as  $\delta r_i^k =$   
 141  $\alpha \sum_j^N (r_{ij}^k / r_{ij}^3) r_{i,o}^2 V_{\text{max}} \Delta t$ , and its constant  $\alpha$  is set to 0.05 according to [34].

142 These intermediate values will then be used to solve the Poisson equation which gives the  
 143 pressure value at the next time-step ( $n + 1$ ). Using this pressure, new velocity and displacement  
 144 vectors are updated as following

$$\nabla \cdot \left( \frac{1}{\rho_i^*} \nabla p_i^{(n+1)} \right) = \frac{\nabla \cdot \vec{V}_i^*}{\Delta t}, \quad (21)$$

$$\nabla \cdot \vec{V}_i^{(n+1)} = \vec{V}_i^* - \frac{1}{\rho_i^*} \nabla p_i^{(n+1)} \Delta t, \quad (22)$$

$$\vec{r}_i^{(n+1)} = \vec{r}_i^{(n)} + 0.5(\vec{V}_i^{(n)} + \vec{V}_i^{(n+1)}) \Delta t + \delta \vec{r}_i^{(n)}. \quad (23)$$

## 147 5. Results

### 148 5.1. Validation and convergence

149 To ensure a suitable particle resolution based on the numerically computed pressure jump  
 150 across the interface, in Fig.2 the data is represented for  $60 \times 60$ ,  $100 \times 100$  and  $140 \times 140$  grids. To  
 151 study numerical convergence, a droplet with the radius of  $r = 0.01$  [m] is situated at the center  
 152 of a square domain, *i.e.*  $x_o/r = y_o/r = 2$ , with the side lengths of  $x/r = y/r = 4$  (see Fig.  
 153 1). While the Dirichlet (no-slip) boundary condition is set for the velocity at all four boundaries,  
 154 namely,  $BC-X_1$ ,  $BC-X_2$ ,  $BC-Y_1$ , and  $BC-Y_2$ , the Neumann boundary condition is applied for the  
 155 pressure field. As for the hydrodynamics properties, we keep both viscosity and density ratios  
 156 equal to unity such that  $\rho_1 = \rho_2 = 1000$  [kg/m<sup>3</sup>] and  $\mu_1 = \mu_2 = 0.1$  [Pa.s] and set the  
 157 surface tension to  $\gamma = 0.01$  [N/m], given neither electrical nor gravitational force.



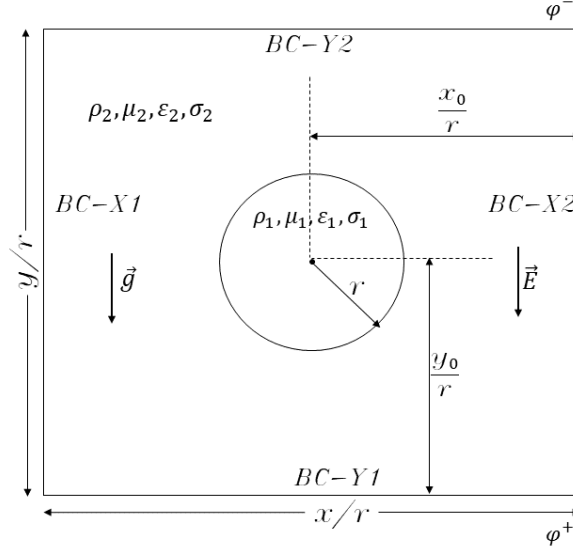


Figure (1) Schematic of the test case for validation and numerical convergence test, bubble rising as well as bubble deformation under the effect of electrohydrodynamics (EHD). For the first test case  $\vec{g} = 0$  and  $\vec{E} = 0$ , for the second one  $\vec{g} \neq 0$  and  $\vec{E} = 0$  while for the third one  $\vec{g} = 0$  and  $\vec{E} \neq 0$

158 This problem, known as Young-Laplace problem, has an analytical solution which is  $\Delta p =$   
 159  $p_i - p_o = \gamma/r = 1$ . As can be seen in Fig.2-Left, the pressure oscillations decrease by increasing  
 160 the resolution from the coarser to the finest and the results, converging towards the analytical  
 161 solution. It is noted that the relative error is less than 1% for the intermediate particle resolution.  
 162 Therefore, we chose the  $100 \times 100$  resolution for our simulations as it provides accurate results  
 163 with reasonable computation cost. Similar simulations, with different surface tension coefficient  
 164 are tested, while putting  $r = 0.5[m]$  and keeping  $x/r$  and  $y/r$  ratios constant to validate the  
 165 accuracy of the used method. As can be seen in Fig.2-Right, the pressure jump increases by an  
 166 increment in the surface tension confirming the capability of the method to capture the physical  
 167 jump across the interface. Once more for the reported simulations, the relative error is less than  
 168 1% when the numerical results are compared to the Laplace's law.

169 It is noteworthy to discuss the reason behind the different values obtained for the theoretical  
 170 and numerical pressure jump at the interface. As mentioned before, the pressure and other flow  
 171 field variables (velocity, color function, etc.) are approximated using the numerical smoothing  
 172 scheme which converts the sharp values at the interface to smoother ones resulting in a loss of  
 173 accuracy and introduction of spurious oscillations near the surface of the droplet. Furthermore,  
 174 it is found that these spurious currents are generated because of an inappropriate evaluation of  
 175 the curvature of the circular droplet due to unreliable values for the unit normal vector ( $\vec{n} =$   
 176  $\frac{\nabla C}{|\nabla C|}$ ) in the surface tension force calculation [37].

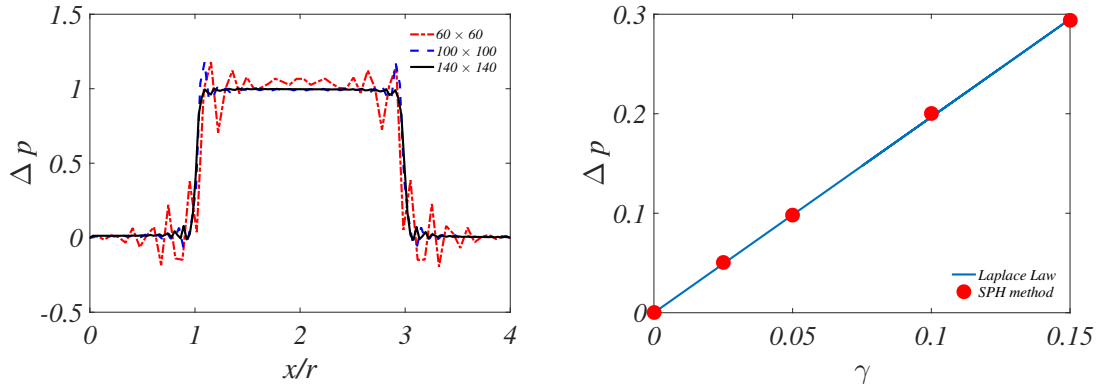


Figure (2) Comparison of (left) the pressure jump across the droplet interface for three particle resolutions and (right) its comparison with the theoretical pressure jump, *i.e.* Laplace's law, for different cases.

### 177 5.2. Bubble rising

178 In this section, the ISPH method is applied to test and to validate the simulation of the  
 179 bubble rising problem due to the gravitational force. The computational geometry for this test  
 180 case is similar to the one shown in Fig. 1 except that the domain size is increased in the normal  
 181 direction (**orthogonal**), *i.e.*  $x/r = 6$  and  $y/r = 12$ , and the bubble is initially placed such  
 182 that  $x_o/r = 3$  and  $y_o/r = 2.4$ . The grid resolution is set to  $240 \times 480$  in  $x$  and  $y$  direction,  
 183 respectively. The velocity boundary conditions are set to be free slip for  $BC - X1$  and  $BC - X2$ ,  
 184 and no slip for  $BC - Y1$  and  $BC - Y2$ . Also, pressure boundary conditions are set to be Dirichlet  
 185 with a constant value at  $BC - Y2$  and Neumann for the other three boundaries ( $\nabla p \cdot \vec{n} = 0$ )  
 186 where  $\vec{n}$  is normal direction to the given boundary.

187 Here, both bubble and bulk phases are set to have stationary conditions at initial time step.  
 188 The bubble **starts** to rise during the simulation **due to** the gravitational forces. This problem can  
 189 be characterized by **Reynolds** and **Bond** numbers defined as following:

$$190 \quad Re = \frac{\rho_2 g^{0.5} (2r_o)^{1.5}}{\mu_2}, \quad (24)$$

and

$$191 \quad Bo = \frac{\rho_2 g (2r_o)^2}{\gamma}. \quad (25)$$

192 respectively.

193 For the first simulation, a case with low density and viscosity **ratios** and high surface tension  
 194 is considered, where  $\rho_2/\rho_1 = 10$  with  $\rho_1 = 100$  [kg/m<sup>3</sup>],  $\mu_2/\mu_1 = 10$  with  $\mu_1 = 1$  [Pa.s],  
 and surface tension coefficient is  $\gamma = 24.5$  [N/m]. Additionally, the gravity is set to be  $\vec{g} =$

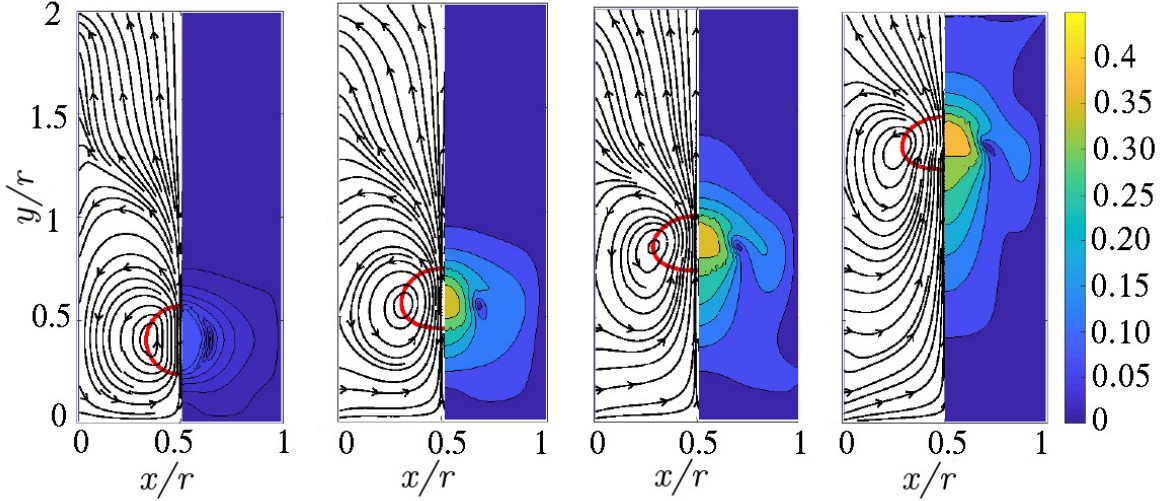


Figure (3) Time evolution of bubble rising problem with the density ratio of  $\rho_1/\rho_2 = 0.1$  and viscosity ratio of  $\mu_1/\mu_2 = 0.1$  at different dimensionless times  $t^* = 0.5$ ,  $t^* = 18.5$ ,  $t^* = 37$  and  $t^* = 64.8$ . Here the dimensionless time is defined as  $t^* = t\sqrt{(g/D)}$  and Reynolds and Bond numbers are  $Re = 35$  and  $Bo = 10$ , respectively. The left half of each snapshot shows the velocity streamlines in black and the droplet interface in red, while the right half shows the velocity magnitude's 'to highest levels' contour in the range of  $[0, 4.5]$  [m/s].

195  $-1$  [m/s<sup>2</sup>] in  $y$  direction such that it produces Reynolds number  $Re = 35$ , and the Bond num-  
 196 ber  $Bo = 10$  for this case. The time snapshot of this test case for dimensionless times of  $t^* = 0.5$ ,  
 197  $t^* = 18.5$ ,  $t^* = 37$  and  $t^* = 64.8$  are shown in Fig. 3. As observed in this figure, the bubble  
 198 starts to rise straight upwards due to the gravity, while its velocity increases from zero to 0.36  
 199 [m/s] and remains constant until it feels the pressure coming from the stationary upper-wall.  
 200 Additionally, the bubble shape is changing from circular shape to a quasi elliptical one due to  
 201 hydrodynamic pressures on its tip. The final shape comes from the competition among surface  
 202 tension, gravitational, and viscous forces. As it is observed, the shape remains unchanged after  
 203 some time steps which is the main reason for the bubble's almost constant terminal velocity.

204 Fig. 4 shows the mean migration velocity and the position of the droplet with respect to  
 205 dimensionless time  $t^* = t\sqrt{(g/D)}$ , which are in agreement with the results of [31] and [38].  
 206 Here, the velocity gradient near the stationary wall starts to deviate at the final times which  
 207 could be due to the confinement effects.

208 To show the applicability of the proposed algorithm for capturing larger deformations and  
 209 breakups, we perform a second bubble rising test case. This time, the computational domain  
 210 size is  $x/r = 6$  and  $y/r = 10$  with the particle resolution of  $240 \times 400$ . The bubble is initially  
 211 placed at  $x_o/r = 3$  and  $y_o/r = 2$ . Here, all four boundaries have no slip boundary condition for

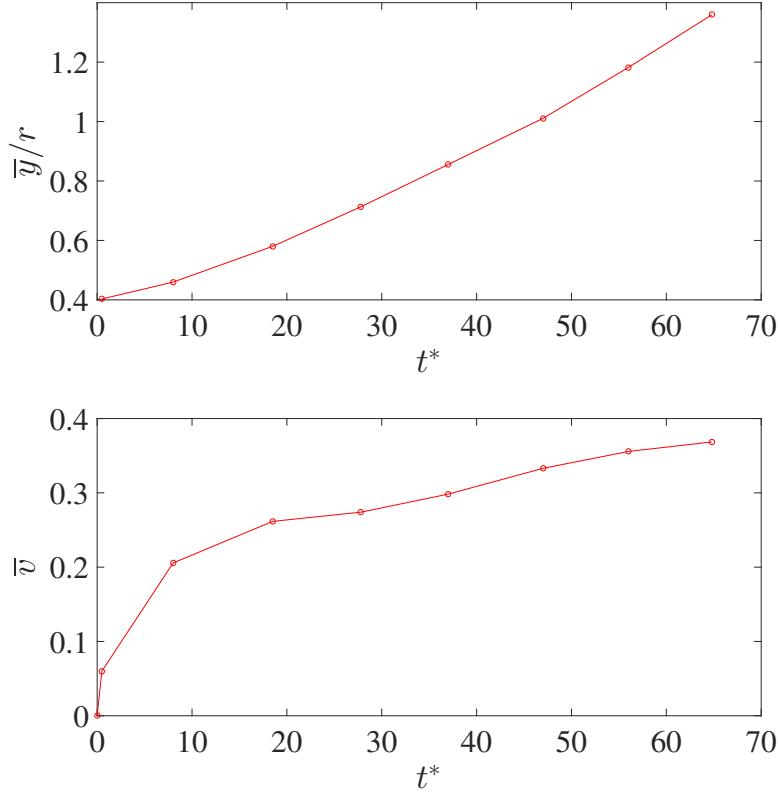


Figure (4) The average normalized central position of the droplet,  $\bar{y}$  (top) and its average vertical migration velocity,  $\bar{v}$  (bottom) as a function of dimensionless time,  $t^*$ .

212 velocity. However, the pressure boundary conditions are kept the same as before. The gravity  
 213 is selected as  $\vec{g} = -1[\text{m/s}^2]$  in  $y$  direction, while the surface tension coefficient is set to be  
 214  $\gamma = 20 [\text{N/m}]$ . Additionally, the density and viscosity ratios are  $\rho_2/\rho_1 = 1000$  and  $\mu_2/\mu_1 =$   
 215  $2.828/10$  with  $\rho_1 = 1 [\text{kg/m}^3]$  and  $\mu_1 = 1 [\text{Pa}\cdot\text{s}]$ , respectively. These choices are for mimicking  
 216 the test case presented in [15] in order to produce the fluid flow system with Reynolds and Bond  
 217 numbers of  $Re = 1000$  and  $Bo = 200$ , respectively.

218 The snapshots of our current simulations are illustrated (middle) in Fig. 5 for the dimension-  
 219 less times between  $t^* = 3.2$  and  $t^* = 5.6$  with a time increment of  $\Delta t^* = 0.4$ . These snapshots  
 220 are compared to their experimental (top) and Volume of Fluid method (bottom) counterparts,  
 221 presented in [39] and [40], respectively. As can be seen, the proposed ISPH approach can predict  
 222 the large deformation and bubble breakup as accurate as its well establish mesh based method.  
 223 The presented Volume of fluid (VoF) method uses a hybrid VoF-level-set method [40] to accu-  
 224 rately capture the interface.

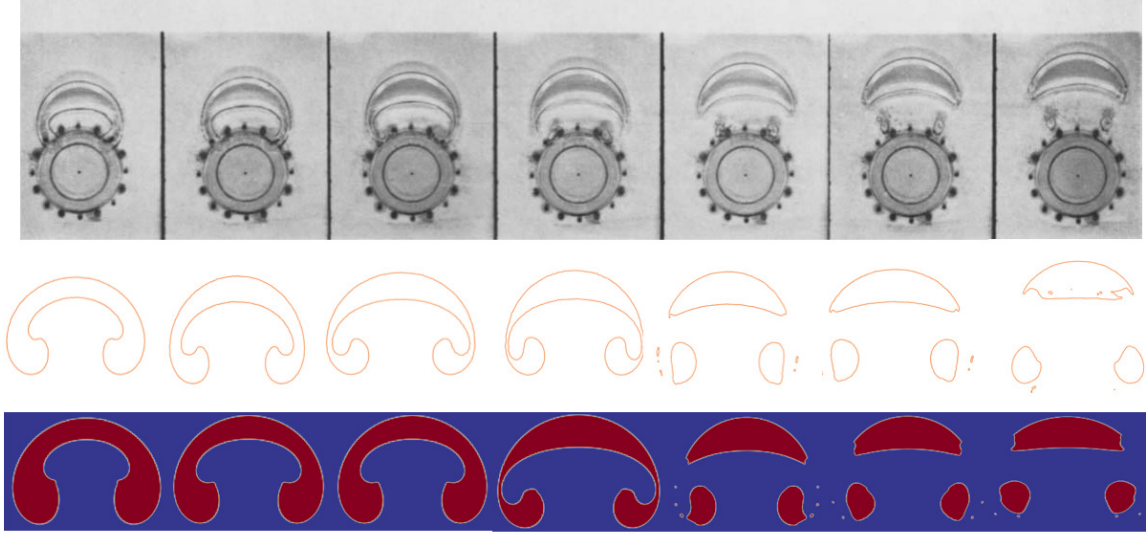


Figure (5) Comparison of bubble rising and break up due to gravitational and hydrodynamic forces using experiment [39], SPH method and Volume of Fluid method [40], respectively from top to bottom rows. Here, the density ratio  $\rho_2/\rho_1 = 1000$  and viscosity ratio  $\mu_2/\mu_1 = 10$  are applied. Reynolds and Bond numbers, as previously defined, are  $Re = 1000$  and  $Bo = 200$ , respectively. The dimensionless time is defined as  $t^* = t\sqrt{g/r_o}$ , starting from  $t^* = 3.2$  at the very first frame on the left, up to  $t^* = 5.6$ , with a time increment of 0.4 per frame.

### 225 5.3. EHD droplet deformation

226 In this section, we consider a suspended circular droplet under the effect of an external applied electric field. The schematic of the computational domain is similar to what is presented  
 227 in Fig. 1 with an increment in the size of the domain. Here, we double the domain size in each  
 228 direction, *i.e.*  $x/r = 8$  and  $y/r = 8$ , in order to reduce the confinement effect. In Fig. 6-left,  
 229 a particle resolution of  $240 \times 240$  is used **with a circular droplet initially placed at the center of**  
 230 **computational domain**. The initial zero velocity are assigned to both fluids and wall particles.  
 231 Density ratio and viscosity ratio are set to unity with values of  $\rho_1 = \rho_2 = 1000$  [kg/m<sup>3</sup>] and  
 232  $\mu_1 = \mu_2 = 1$  [Pa.s]. The surface tension coefficient  $\gamma = 1$  [N/m]. The velocity and pressure  
 233 boundary conditions are exactly the same as those imposed in section 5.1. The electrical bound-  
 234 ary conditions are Dirichlet ( $\varphi = cte.$ ) and Neumann boundary ( $\nabla\varphi \cdot \vec{n} = 0$ ) conditions for  
 235 horizontal (*i.e.*  $BC - Y1$  and  $BC - Y2$ ) and vertical walls (*i.e.*  $BC - X1$  and  $BC - X2$ ), respec-  
 236 tively, where  $\vec{n}$  is normal direction to the given boundary.  
 237

238 The deformation of a suspended circular droplet under such conditions is a commonly uti-  
 239 lized test case for validation of a EHD solver, where two theories are available in the literature.  
 240 Taylor [41] estimates the droplet deformation  $D_T$  as

$$D_T = \frac{9f_d\tau E_o^2 \epsilon_2 r_o}{8(2 + R)^2 \gamma}, \quad (26)$$

241 where  $f_{dT}$  is the discriminating function evaluated as

$$f_{dT} = R^2 + 1 - 3.5S + 1.5R. \quad (27)$$

242 For the same problem, Feng [42] suggests the following relation

$$D_F = \frac{f_{dF} E_o^2 \epsilon_1 r_o}{3(1+R)^2 S \gamma}, \quad (28)$$

243 where  $f_{dF}$  is estimated from

$$f_{dF} = R^2 + 1 - 3S + R. \quad (29)$$

244 In Eqs. (26) and (28),  $r_o$  is the initial droplet radius before its deformation and  $E_o$  is the  
 245 electric field intensity in vertical direction which is calculated from  $E_o = (\varphi^+ - \varphi^-)/H$ ,  $H$  being  
 246 the domain height. Additionally, the permittivity ratio and the conductivity ratio of droplet to  
 247 the bulk are called  $S$  and  $R$ , presented as

$$S = \frac{\epsilon_1}{\epsilon_2}, \quad R = \frac{\sigma_1}{\sigma_2}, \quad (30)$$

248 where  $\epsilon$  and  $\sigma$  are the electrical permittivity and conductivity, respectively. Also the subscripts  
 249 1 and 2 show, droplet and bulk medium properties, respectively.

250 Another point in the theory of droplet deformation is to investigate the velocity recirculation  
 251 vectors inside and outside of the droplet when a vertical electric field is applied. The relative  
 252 differences in the electric permittivity and conductivity of both constituent phases define the  
 253 direction of the flow rotation in either phase. This is shown for two cases in Fig. 6. On the left  
 254 side test case is adopted for  $S = 0.5$  and  $R = 0.05$  with the electrical permittivity of the droplet  
 255 ( $\epsilon_1$ ) being 0.5 [F/m] which is half of that of the bulk fluid. Also, the electrical conductivity of  
 256 the droplet ( $\sigma_1$ ) is set to 150 [S/m] which is three-times more than the background fluid. On  
 257 the right side of Fig. 6, the test case has  $S = 0.5$  and  $R = 3$  with  $\epsilon_1 = 0.5$  and  $\sigma_1 = 1$ . As can  
 258 be seen in the left sub-figure, the re-circulation zone in the first quarter (i.e. the top-right quarter  
 259 inside the droplet) of the droplet orients clockwise. This should be the case for  $S > R$  and is  
 260 consistent with the results of [29]. The opposite flow circulation pattern should be expected for  
 261 the case of  $S < R$  as it also presented on the right side of the same figure.

262 Additionally, Eqs. (27) and (29) define the sign of Eqs. (26) and (28), respectively. The pos-  
 263 itive sign, so called prolate deformation, indicates that the droplet is elongated in the direction  
 264 parallel to the electric field. The positive sign, so called oblate deformation, shows the droplet  
 265 elongation in the opposite direction. For the comparison with the simulation results, we define  
 266 the numerical deformation as

$$D_N = \frac{A - B}{A + B}, \quad (31)$$



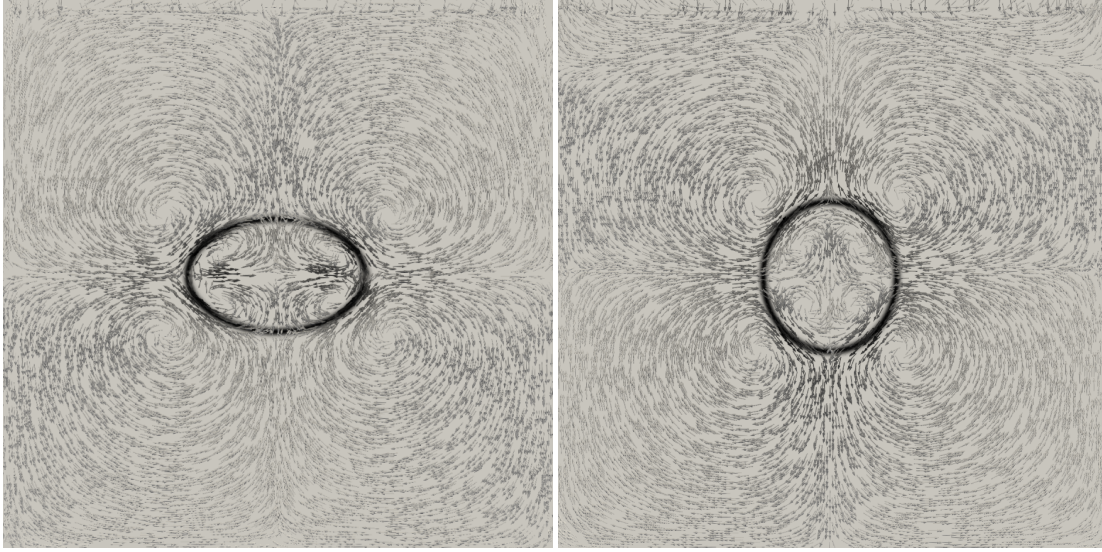


Figure (6) Deformation of a suspended droplet in response to an external vertical electric field in the steady-state simulation for the cases with (left)  $S = 0.5$ ,  $R = 0.05$  and (right)  $S = 0.5$ ,  $R = 3$ .

267 where  $A$  and  $B$  are the elliptic droplet diameters, parallel and perpendicular to the direction of  
 268 the external electric field, respectively, at the steady state condition. When this parameter is equal  
 269 to zero, the droplet keeps its initial circular shape. On the other hand, more deviation from zero  
 270 indicates more deformation from its initial shape.

271 Fig. 7 provides comparison between the current ISPH results and the two aforementioned  
 272 theories for multiple cases. As can be seen, numerical data reasonably follow the available theo-  
 273 ries. However, in most of the cases, an over-prediction is reported by the simulations. Some  
 274 might be some possible reasons for such behaviour can be mentioned: (i) in the theory it is as-  
 275 sumed that the droplet remains circular even after applying the electric field. This means the  
 276 change in the curvature is not integrated in the deformation equation, but only the surface ten-  
 277 sion coefficient. (ii) Another reason might be due to the confinement effect. In theories, it is  
 278 assumed that the droplet is suspended in an unbounded domain for simplicity. However, pro-  
 279 viding such domain numerically, or even with twice larger computational domain, is very ex-  
 280 pensive computationally. Finally, the hydrodynamical properties of droplets such as density and  
 281 viscosity are not taken into account theoretically and the problem is considered to be *inviscid*.

#### 282 5.4. Couette Flow

283 This section investigates the deformation of a droplet suspended between two parallel plates  
 284 subjected to a constant shear. The flow configuration, known as Couette flow, is presented in  
 285 Fig. 8. In this case, the flow is driven by viscous forces or pressure gradients [43]. Different cases

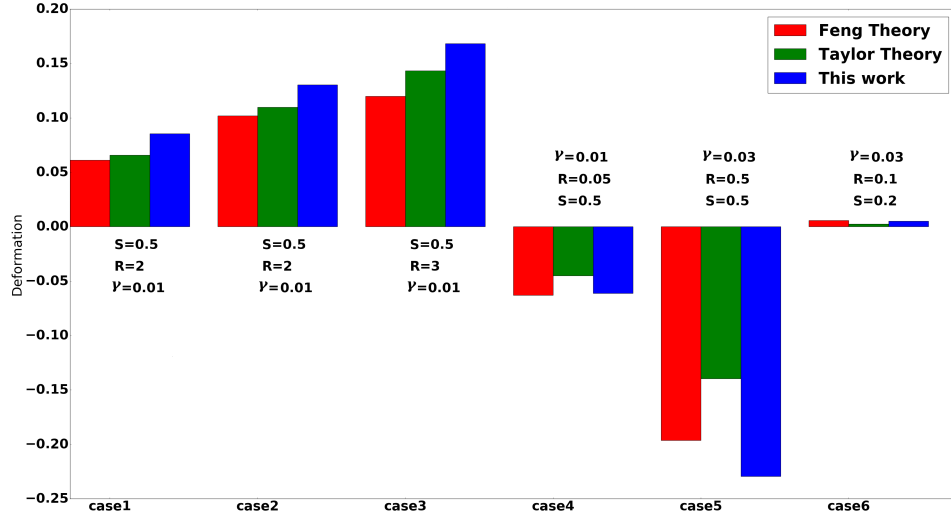


Figure (7) Comparison of deformation for all cases. permittivity ratio, conductivity ratio and surface tension coefficient of each simulation,  $S$ ,  $R$ ,  $\gamma$ , respectively, mentioned below or above the corresponding case.

286 with and without an external electric field with the magnitude of unity perpendicular to the flow  
 287 direction are simulated.

288 The computational domain consists of a rectangle box with the size of  $x/r = 16$  and  $y/r =$   
 289  $4$  discretized by a set of initially equally spaced  $400 \times 100$  particles, arranged in a Cartesian grid.  
 290 The two-phase system contains a droplet with the initial radius of  $r_o$ , placed in the middle of the  
 291 domain, and the bulk fluid with the same density of  $\rho_1 = \rho_2 = 1000$  [kg/m<sup>3</sup>] and the dynamic  
 292 viscosity of  $\mu_1 = \mu_2 = 0.2$  [Pa.s]. The velocity boundary conditions are set to Dirichlet (no-  
 293 slip) on the plates (*i.e.*  $BC - Y1$  and  $BC - Y2$ ) and periodic for the inlet and outlets (*i.e.*  $BC - X1$   
 294 and  $BC - X2$ ). The pressure boundary conditions is Dirichlet  $BC - Y2$  and Neumann for the  
 295 rest of boundaries. Also, the boundary conditions for electrical potential are of Dirichlet at the  
 296 walls (*i.e.*  $\varphi = cte$  in  $BC - Y1$  and  $BC - Y2$ ) and periodic for the two other sides (*i.e.*  $BC - X1$   
 297 and  $BC - X2$ ).

298 Initially, the upper and the lower wall velocities are set to  $U_o/2$  and  $-U_o/2$ , respectively,  
 299 where  $U_o = 0.02$  [m/s]. Additionally, particles inside the droplet are initialized to be at rest,  
 300 while background fluid particles having undisturbed Couette flow velocity. The simulations  
 301 are performed for a range of electrical permittivity and electrical conductivity ratios shown as  
 302 ( $S$ ,  $R$ ), while neglecting the gravity and keeping the surface tension coefficient constant  $\gamma =$   
 303  $0.02$  [N/m]. The droplet radius is a quarter of the distance between two parallel plates (*i.e.*  
 304  $r = H/4$ ). The dimensionless Reynolds, Weber and **Electroinertial** numbers, respectively, are



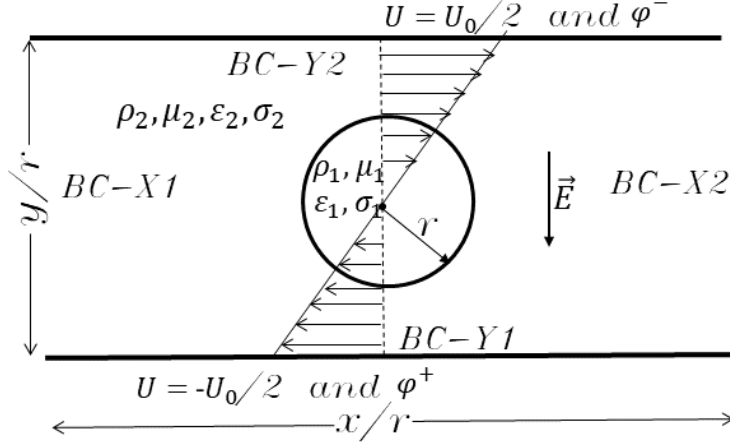


Figure (8) Schematic of the Couette flow test case.

305 as follows

$$Re = \frac{\rho_2 U_0 r_o}{\mu_2}, \quad We = \frac{\rho_2 U_0^2 r_o}{\gamma}, \quad Ei = \frac{\rho_2 U_0^2}{\epsilon_2 E_0^2}, \quad (32)$$

306 where  $Re = 1$ ,  $We = 0.2$ , and  $Ei = 50$ .

307 Fig.9 shows the time evolution of the droplets' deformation under the same external electric  
 308 field and the shear stress conditions, but for different working fluids having different electrical  
 309 permittivity and conductivity ratios (*i.e.* only a change in  $S$  and  $R$  is considered here). In this  
 310 figure, the **dimensionless** time is defined as  $t^* = tU_0/r_o$ , while the droplet deformation is calcu-  
 311 lated from

$$D_f = \frac{L_{max} - L_{min}}{L_{max} + L_{min}}, \quad (33)$$

312 where  $L_{max}$  and  $L_{min}$  are major and minor droplet diameters, respectively. As can be seen in  
 313 this figure, the droplet deformation increases when an external electric field is applied regardless  
 314 of  $S$  and  $R$ . Additionally, at the constant electrical permittivity ratio, larger deformations can  
 315 be achieved by an increment in the electrical conductivity ratio when  $S > R$ . However, for  
 316 the similar condition (*i.e.*  $S = cte.$ ), smaller deformations are seen by an increment in the  
 317 electrical conductivity ratio when  $S < R$ . Similarly, at constant electrical conductivity ratio  
 318 larger electrical permittivities result in larger droplet deformations for  $R < S$ , while decreases the  
 319 same for  $S < R$ . It is noted that the (5.0, 0.2) and (5.0, 0.5) test problems did not reach a steady  
 320 profile during the simulation time, here fixed at  $t^* = 1$  due to large computational costs. Fig.  
 321 10 provides a comparison on the interface shape in the absence (in blue) and the presence of the  
 322 electric field (in black) at this time. Following the previous figure, it can be seen that the droplets  
 323 are more slender for larger deformation factors.

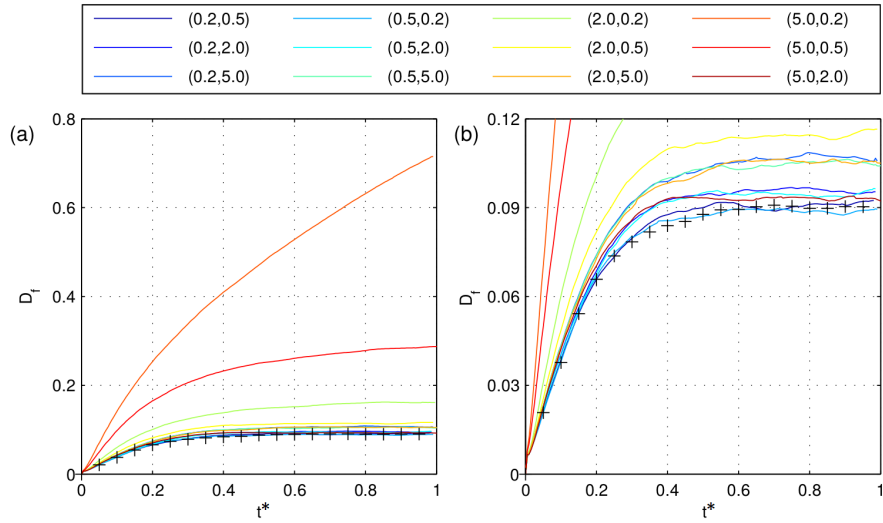


Figure (9) Numerical deformation for twelve cases (Left), a close-up look at the rate of deformation at the steady state (Right). Cases without electric field are denoted by a black + sign. The pair number on the legend box, corresponds to the electrical permittivity and electrical conductivity ( $S, R$ ), respectively.

324 It is notable that the angle between the major axis of the elliptic droplet and the stream-wise  
 325 direction become smaller with an increment in the conductivity ratio, while the cases of  $(5.0, 0.2)$   
 326 and  $(5.0, 0.5)$  are immediately distinguishable due to their larger deformations. This elongation  
 327 is due to the suppression of surface tension forces which is the result of the larger electric field  
 328 force at higher electrical conductivity ratios. It is also noted that the droplet is no longer elliptical  
 329 and is suspected to have the breakup at larger time steps.

330 Finally, the time snapshot of an extreme test case with the electrical permittivity ratio of  $S =$   
 331 10 and the electrical conductivity ratio of  $R = 0.2$  is illustrated in Fig. 11 to show the ability of  
 332 the presented method to capture very large deformations with the interfacial topological change.  
 333 Here, the interface is represented by red color, while the velocity streamlines and electrical vectors  
 334 are represented by blue and black arrows, respectively. In this case, the circular droplet becomes  
 335 elliptical soon after the start of the simulation. The elliptical interface is elongated in the stream-  
 336 wise axis direction due to the four re-circulation zones in the bulk flow just next to the interface.  
 337 Soon after that, pairs of re-circulation merge with each other at the both tips of the droplet and  
 338 cause the creation of the third re-circulation in its center. By time, the droplet gets folded in  
 339 four different places and new re-circulation zones appear close to the interface which makes the  
 340 droplet very susceptible to breakup. As can be seen, this is a promising test problem to show  
 341 the ability of the present ISPH code to treat the complex multi-phase fluid behavior under an  
 342 extreme EHD conditions with large interfacial deformation.

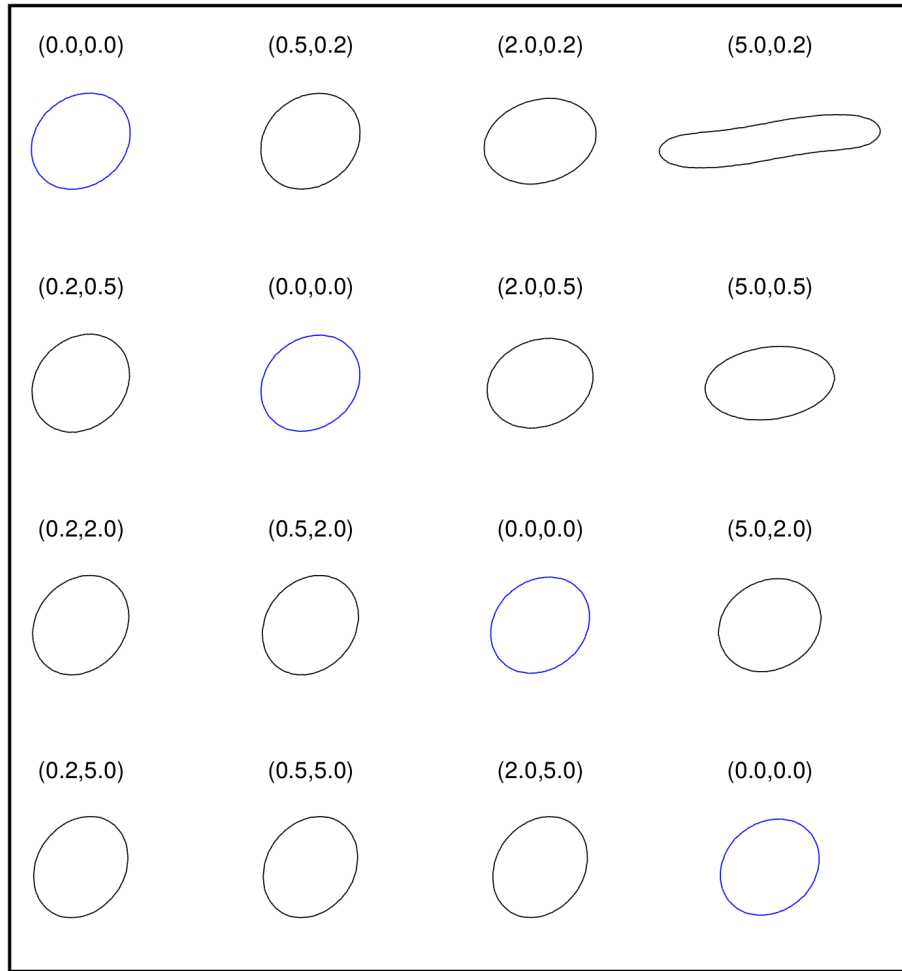


Figure (10) Bubble interface at  $t^* = 1$ . The pair number above each case corresponds to the electrical permittivity and electrical conductivity ( $S, R$ ), respectively. If zero, the electric field is not applied.

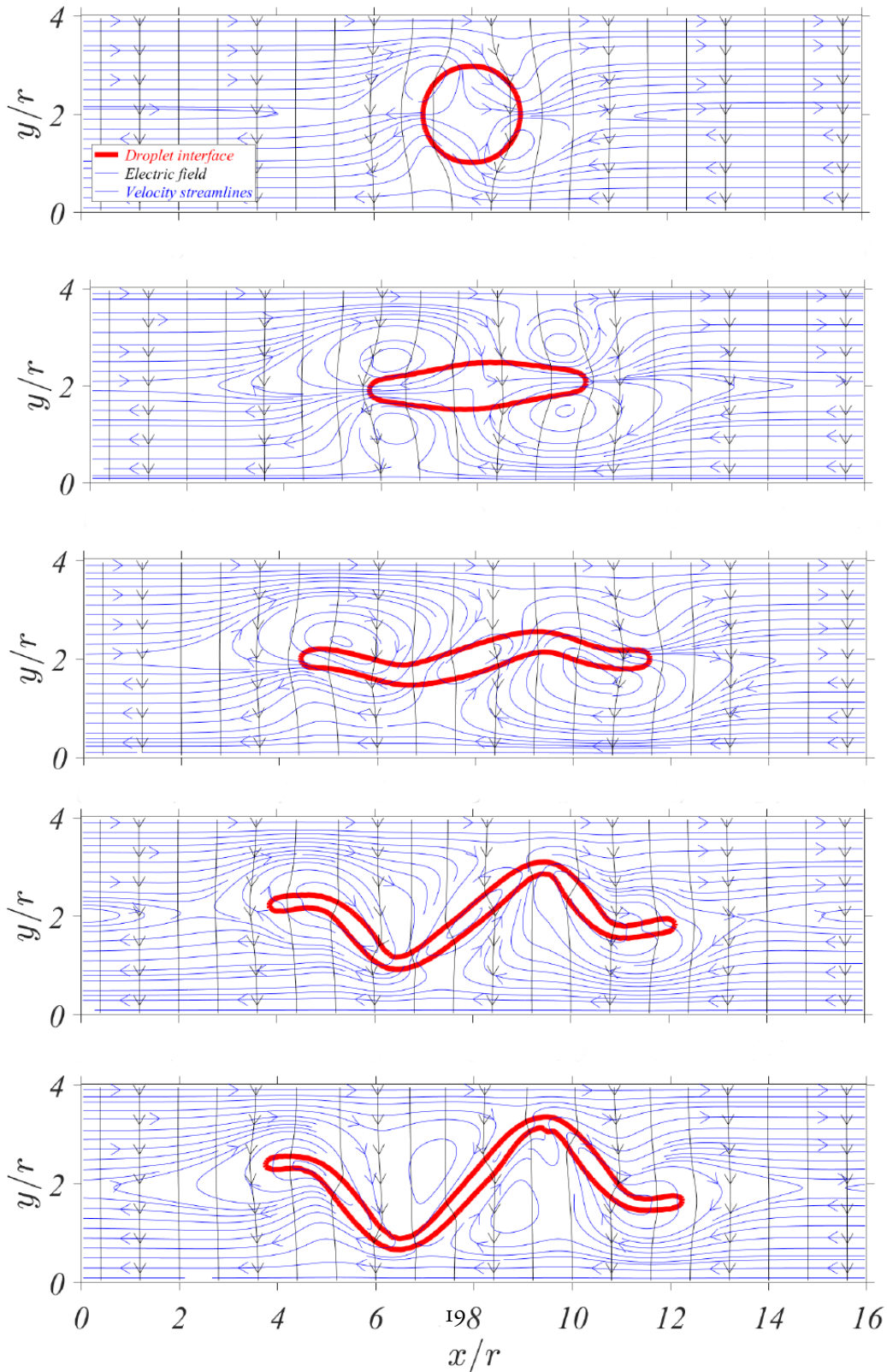


Figure (ii) Deformation of a suspended droplet in Couette flow with  $S = 10$  and  $R = 0.2$  subject to electric field at  $t^* = 0, t^* = 0.4, t^* = 0.8, t^* = 1.2$  and  $t^* = 1.6$ , respectively, from top to bottom where dimensionless time is defined by  $t^* = tU_o/r$ . The velocity streamlines (in blue), the electric field vectors (in black) and the droplet interface (in red) are shown at five moments.

## 343 6. Summary

344 In this work, we presented an effective multi-phase Incompressible Smoothed Particle Hy-  
345 drodynamics (ISPH) approach to simulate complex multi-physics electrohydrodynamics (EHD)  
346 problems. We showed a step-by-step validation of the multiphase code for surface tensions, hy-  
347 drodynamic forces and electric forces, respectively, by solving Laplace's law, bubble rising and  
348 buoyant droplet deformation under an applied electric field problems. Results are validated  
349 either against available analytical or numerical results. An overall satisfactory agreement were  
350 found. Finally, we presented, for the first time, results of droplet deformation under sheared  
351 Couette flow with external electric field for a range of simulation parameters. Different param-  
352 eters such as time resolved topological changes, droplet deformation magnitudes as well as velocity  
353 field and electrical potential vectors were presented and compared with each other. It was shown  
354 that the current ISPH approach is able to be easily adopted for different multi-physics problems.  
355 It is also capable of predicting large interfacial topological changes such as folding and breakup.  
356 In future, **our strategy would be to include** more complex transport and multi-physics phenom-  
357 ena.

## 358 Acknowledgment

359 This work has benefited from the financial support of TOTAL SA within the framework  
360 of a call for projects with exploratory projects coordinated by TOTAL SA and the CNRS. The  
361 authors also acknowledge the access to French HPC resources provided by the French regional  
362 computing center of Normandy CRIANN (2017002). The first author acknowledges the fi-  
363 nancial supports provided by Normandy region. The second author acknowledge the support  
364 provided by Alexander von Humboldt Foundation through the project FRA-1204799-HFST-E  
365 for the experienced researcher.

## 366 References

- 367 [1] Q. Xiong, S.-C. Kong, High-resolution particle-scale simulation of biomass pyrolysis, ACS  
368 Sustainable Chemistry & Engineering 4 (2016) 5456–5461.
- 369 [2] M. Sarafraz, M. S. Shadloo, Z. Tian, I. Tlili, T. A. Alkanhal, M. R. Safaei, M. Goodarzi,  
370 M. Arjomandi, Convective bubbly flow of water in an annular pipe: Role of total dissolved  
371 solids on heat transfer characteristics and bubble formation, Water 11 (2019) 1566.
- 372 [3] A. Izadi, M. Siavashi, Q. Xiong, Impingement jet hydrogen, air and cuh<sub>2</sub>o nanofluid cool-  
373 ing of a hot surface covered by porous media with non-uniform input jet velocity, Inter-  
374 national Journal of Hydrogen Energy 44 (2019) 15933–15948.

- 375 [4] M. V. Bozorg, M. H. Doranehgard, K. Hong, Q. Xiong, Cfd study of heat transfer and  
376 fluid flow in a parabolic trough solar receiver with internal annular porous structure and  
377 synthetic oil–al<sub>2</sub>o<sub>3</sub> nanofluid, *Renewable Energy* 145 (2020) 2598–2614.
- 378 [5] M. Y. A. Jamalabadi, M. DaqiqShirazi, A. Kosar, M. S. Shadloo, Effect of injection angle,  
379 density ratio, and viscosity on droplet formation in a microfluidic t-junction, *Theoretical  
380 and Applied Mechanics Letters* 7 (2017) 243–251.
- 381 [6] R. Sadeghi, M. S. Shadloo, M. Hopp-Hirschler, A. Hadjadj, U. Nieken, Three-  
382 dimensional lattice boltzmann simulations of high density ratio two-phase flows in porous  
383 media, *Computers & Mathematics with Applications* 75 (2018) 2445–2465.
- 384 [7] R. A. Gingold, J. J. Monaghan, Smoothed particle hydrodynamics: theory and application  
385 to non-spherical stars, *Monthly notices of the royal astronomical society* 181 (1977) 375–389.
- 386 [8] L. B. Lucy, A numerical approach to the testing of the fission hypothesis, *The astronomical  
387 journal* 82 (1977) 1013–1024.
- 388 [9] M. S. Shadloo, A. Zainali, S. H. Sadek, M. Yildiz, Improved incompressible smoothed par-  
389 ticle hydrodynamics method for simulating flow around bluff bodies, *Computer methods  
390 in applied mechanics and engineering* 200 (2011) 1008–1020.
- 391 [10] M. S. Shadloo, A. Zainali, M. Yildiz, A. Suleman, A robust weakly compressible sph  
392 method and its comparison with an incompressible sph, *International Journal for Nu-  
393 merical Methods in Engineering* 89 (2012) 939–956.
- 394 [11] M. Hirschler, P. Kunz, M. Huber, F. Hahn, U. Nieken, Open boundary conditions for  
395 isph and their application to micro-flow, *Journal of Computational Physics* 307 (2016)  
396 614–633.
- 397 [12] S. Marrone, M. Antuono, A. Colagrossi, G. Colicchio, D. Le Touzé, G. Graziani,  $\delta$ -sph  
398 model for simulating violent impact flows, *Computer Methods in Applied Mechanics and  
399 Engineering* 200 (2011) 1526–1542.
- 400 [13] M. S. Shadloo, R. Weiss, M. Yildiz, R. A. Dalrymple, et al., Numerical simulation of long  
401 wave runup for breaking and nonbreaking waves, *International Journal of Offshore and  
402 Polar Engineering* 25 (2015) 1–7.
- 403 [14] H. Gotoh, A. Khayyer, On the state-of-the-art of particle methods for coastal and ocean  
404 engineering, *Coastal Engineering Journal* 60 (2018) 79–103.

- 405 [15] A. Zainali, N. Tofighi, M. S. Shadloo, M. Yildiz, Numerical investigation of newtonian  
406 and non-newtonian multiphase flows using isph method, *Computer Methods in Applied*  
407 *Mechanics and Engineering* 254 (2013) 99–113.
- 408 [16] N. Grenier, M. Antuono, A. Colagrossi, D. Le Touzé, B. Alessandrini, An hamiltonian  
409 interface sph formulation for multi-fluid and free surface flows, *Journal of Computational*  
410 *Physics* 228 (2009) 8380–8393.
- 411 [17] M. S. Shadloo, M. Yildiz, Numerical modeling of kelvin–helmholtz instability using  
412 smoothed particle hydrodynamics, *International Journal for Numerical Methods in Engi-*  
413 *neering* 87 (2011) 988–1006.
- 414 [18] C. Ulrich, M. Leonardi, T. Rung, Multi-physics sph simulation of complex marine-  
415 engineering hydrodynamic problems, *Ocean Engineering* 64 (2013) 109–121.
- 416 [19] M. Hopp-Hirschler, M. S. Shadloo, U. Nieken, Viscous fingering phenomena in the early  
417 stage of polymer membrane formation, *Journal of Fluid Mechanics* 864 (2019) 97–140.
- 418 [20] M. Hopp-Hirschler, M. S. Shadloo, U. Nieken, A smoothed particle hydrodynamics ap-  
419 proach for thermo-capillary flows, *Computers & Fluids* 176 (2018) 1–19.
- 420 [21] M. Shadloo, G. Oger, D. Le Touzé, Smoothed particle hydrodynamics method for fluid  
421 flows, towards industrial applications: Motivations, current state, and challenges, *Com-*  
422 *puters & Fluids* 136 (2016) 11–34.
- 423 [22] M. Rezavand, M. Taeibi-Rahni, W. Rauch, An isph scheme for numerical simulation of  
424 multiphase flows with complex interfaces and high density ratios, *Computers and Mathe-*  
425 *matics with Applications* 75 (2018) 2658 – 2677.
- 426 [23] Y. Hu, D. Li, X. Niu, Y. Zhang, Lattice boltzmann model for the axisymmetric electro-  
427 thermo-convection, *Computers and Mathematics with Applications* 78 (2019) 55 – 65.
- 428 [24] J. Weirather, V. Rozov, M. Wille, P. Schuler, C. Seidel, N. A. Adams, M. F. Zaeh, A  
429 smoothed particle hydrodynamics model for laser beam melting of ni-based alloy 718,  
430 *Computers and Mathematics with Applications* (2018).
- 431 [25] K. Abdella, H. Rasmussen, I. Inculet, Interfacial deformation of liquid drops by electric  
432 fields at zero gravity, *Computers and Mathematics with Applications* 31 (1996) 67 – 82.
- 433 [26] X. Huang, L. He, X. Luo, H. Yin, D. Yang, Deformation and coalescence of water droplets  
434 in viscous fluid under a direct current electric field, *International Journal of Multiphase*  
435 *Flow* 118 (2019) 1 – 9.

- 436 [27] Q. Yang, B. Q. Li, Y. Ding, 3d phase field modeling of electrohydrodynamic multiphase  
437 flows, *International Journal of Multiphase Flow* 57 (2013) 1 – 9.
- 438 [28] F. Alberini, D. Dapelo, R. Enjalbert, Y. V. Crombrugge, M. J. Simmons, Influence of dc  
439 electric field upon the production of oil-in-water-in-oil double emulsions in upwards mm-  
440 scale channels at low electric field strength, *Experimental Thermal and Fluid Science* 81  
441 (2017) 265 – 276.
- 442 [29] M. Shadloo, A. Rahmat, M. Yildiz, A smoothed particle hydrodynamics study on the elec-  
443 trohydrodynamic deformation of a droplet suspended in a neutrally buoyant newtonian  
444 fluid, *Computational Mechanics* 52 (2013) 693–707.
- 445 [30] A. Rahmat, M. Yildiz, A multiphase isph method for simulation of droplet coalescence  
446 and electro-coalescence, *International Journal of Multiphase Flow* 105 (2018) 32–44.
- 447 [31] A. Rahmat, N. Tofghi, M. Yildiz, Numerical simulation of the electrohydrodynamic ef-  
448 fects on bubble rising using the sph method, *International Journal of Heat and Fluid Flow*  
449 62 (2016) 313 – 323.
- 450 [32] A. Rahmat, N. Tofghi, M. Shadloo, M. Yildiz, Numerical simulation of wall bounded  
451 and electrically excited rayleigh–taylor instability using incompressible smoothed particle  
452 hydrodynamics, *Colloids and Surfaces A: Physicochemical and Engineering Aspects* 460  
453 (2014) 60–70.
- 454 [33] M. Liu, G. Liu, K. Lam, Constructing smoothing functions in smoothed particle hydrody-  
455 namics with applications, *Journal of Computational and Applied Mathematics* 155 (2003)  
456 263 – 284.
- 457 [34] M. Shadloo, A. Zainali, M. Yildiz, Simulation of single mode rayleigh–taylor instability  
458 by sph method, *Computational Mechanics* 51 (2013) 699–715.
- 459 [35] J. Brackbill, D. Kothe, Z. CA, A continuum method for modeling surface tension, *Journal*  
460 *of Computational Physics* (1992) 335–354.
- 461 [36] D. Fleisch, *A guide to maxwell equations*, Cambridge University Press (2008).
- 462 [37] M. Sussman, E. G. Puckett, A Coupled Level Set and Volume-of-Fluid Method for Com-  
463 puting 3D and Axisymmetric Incompressible Two-Phase Flows, *Journal of Computational*  
464 *Physics* 162 (2000) 301–337.
- 465 [38] A. Zhang, Z. Guo, Q. Wang, S. Xiong, Three-dimensional numerical simulation of bubble  
466 rising in viscous liquids: A conservative phase-field lattice-boltzmann study, *Physics of*  
467 *Fluids* 31 (2019) 063106.



- 468 [39] J. K. Walters, J. F. Davidson, The initial motion of a gas bubble formed in an inviscid  
469 liquid, *Journal of Fluid Mechanics* 17 (1963).
- 470 [40] A. Asuri Mukundan, T. Ménard, A. Berlemont, J. C. C. Brändle De Motta, R. Eggels,  
471 Validation and Analysis of 3D DNS of planar pre-filming airblast atomization simulations,  
472 in: In Proceedings of ILASS Americas, 30th Annual Conference on Liquid Atomization  
473 and Spray Systems. May 12th-15th, Tempe, Arizona, USA, Tempe, United States.
- 474 [41] G. I. Taylor, A. D. McEwan, L. N. J. de Jong, Studies in electrohydrodynamics. i. the  
475 circulation produced in a drop by an electric field, *Proceedings of the Royal Society of  
476 London. Series A. Mathematical and Physical Sciences* 291 (1966) 159–166.
- 477 [42] J. Q. Feng, Electrohydrodynamic behaviour of a drop subjected to a steady uniform electric  
478 field at finite electric reynolds number, *Proceedings of the Royal Society of London. Series  
479 A: Mathematical, Physical and Engineering Sciences* 455 (1999) 2245–2269.
- 480 [43] Deformation of a droplet in Couette flow subject to an external electric field simulated  
481 using ISPH, PARTICLES, Barcelona, Spain, 2015.